

# Energy saving by reducing motor rating of Sucker-Rod Pump systems

Weicheng Li<sup>a,b</sup>, Vahid Vaziri<sup>b</sup>, Sumeet S Aphale<sup>b</sup>, Shimin Dong<sup>a</sup>, Marian Wiercigroch<sup>b,\*</sup>

<sup>a</sup>*School of Mechanical Engineering, Yanshan University, Qinhuangdao, 066004, China*

<sup>b</sup>*Centre for Applied Dynamics Research, School of Engineering, University of Aberdeen, Aberdeen AB24 3UE, UK*

---

## Abstract

Energy industry can make significant savings by reducing electric motors ratings of the popular Sucker-Rod Pump (SRP) systems. This can be achieved by application of robust controllers, which are fully integrated with the SRP systems. In this work we have developed, modelled and analysed such integrated systems, specifically by examining two control schemes with open- and closed-loop controllers. The open loop scheme employs a genetic algorithm optimizing frequency in order to minimize fluctuations in a motor output power. This approach results in reducing the peak torque and consequently decreases the required motor rating by 20%. However, the scheme relies on a complex model of this electromechanical system, and it is computationally expensive. The second proposed scheme with a closed-loop control, the first of its kind for the SRP systems, is much faster and robust. It allows to reduce the motor rating by further 30% of that required in the open-loop scheme, which can save \$246M through choosing smaller motors and \$39M per year by reducing motor inner loss.

*Keywords:* Sucker-rod pumping system, energy saving, motor control, open and closed-loop frequency control

---

## 1. Introduction

Due to its simplicity, reliability and low cost, a sucker-rod pump system (SRP) is the most popular for generating artificial lift in onshore oil-wells [1–4]. There are typically powered by AC electrical motors and there is nearly 0.7 million SRPs operating all over the world and consequently, improvements to the energy efficiency of these systems lead to a global reduction of a carbon footprint [5–7]. As a result, in addition to the main stream research on enhanced oil recovery [8, 9], two-phase closed thermosyphons [10] and steam assisted gravity drainage [11–13], efficiency improvement schemes for existing SRP mechanisms are in great demand and have attracted a significant research effort.

---

\*Corresponding author.

*Email address:* m.wiercigroch@abdn.ac.uk (Marian Wiercigroch)

One full lift cycle (period of operation) of the SRP can be split into two operational regimes: (i) suction phase (upstroke) - when the oil is sucked from the well and into the barrel and (ii) discharge phase (downstroke) - when the oil is pumped out of the barrel [14]. The suction phase requires a high torque and therefore an electric motor has to supply a higher power. The discharge phase tends to return power back to the motor in the form of a negative torque, which in most cases, is undesirable. To counter this, a balancing weight mechanism is employed [15, 16]. The inclusion of this balancing weight requires the motor to deliver a torque with a double hump profile (i.e. two peaks within a full cycle) [14, 17]. However, these humps are of relatively small duration compared to the period of the full cycle and the motor is required to deliver a significantly lower torque for most part of the lift cycle. However, the higher torque requirement to overcome these humps necessitates a significantly overrated motor to be employed, even though the average torque required throughout the lift cycle can be provided adequately by a motor with a significantly lower rating. An overrated motor comes at the cost of reduced efficiency and lower fatigue life for the surface transmission system [18, 19]. Moreover, the reverse torque generated during the discharge phase (downstroke), forces the motor to behave like a generator; resulting in additional detrimental effects [20, 21]. Consequently, smoothing out the load torque profile by “peak shaving and valley filling” is highly desirable.

Approaches reported in literature to achieve the desirable (i.e. smooth) load torque profile can be broadly grouped into four categories: (i) improved mechanical design of the SRP, for example, the double horse-head [22], the parallel four-bar [23] and the linear electromagnetic approach [24]; (ii) modifications to the existing SRP, for example, by adding a secondary-balance device [22], utilizing high-slip motors [25] and tubular linear induction motors [26]; (iii) swabbing parameters optimization, for example, pumping speed, pumping depth, pump diameter, rod string design and stroke length [27–31] and (iv) employing control techniques via bespoke control circuitry, for example, frequency converters [1, 32, 33], multifunction energy-saving systems [20, 34] and energy feedback devices [35]. Though the improved mechanical design and modifications-based approaches have demonstrated potential in significantly reducing load torque variation, retrofitting or swapping existing, in-service SRPs is deemed unattractive due to the additional costs resulting from bespoke design requirements and production loss, due to the prohibitive downtime required to install the required modifications. Consequently, due to significant improvements in the electrical and electronic components associated with real-time control circuitry, their relatively low cost and loss of production implications, adopting suitable control algorithms to smoothen out the load torque profile is seen as the most desirable way forward and subsequently, has garnered a considerable research interest.

With recent strides in electronics and associated technology, financially viable frequency conversion and control techniques have been proposed [36–39]. These techniques are capable of automatically adjusting the strokes-per-minute (SPM) pumping rate that was traditionally achieved through manual adjustments, [1, 40]. Over the years, the open-loop frequency conversion control method has undergone several improvements. Dual pulse width modulation (PWM) frequency conversion, capable of independently controlling the speed of the motor during the upstroke (slow) and downstroke (fast) was reported in [32]. Inertial load distribution was utilized to effectively reduce load variation via real-time adjustment of motor speed, [41, 42]. However, a systematic method for selecting the optimal speed curve that matches the load has not yet been formalized. Frequency optimization based on the SRP system model via constant  $V/F$  control was proposed in [43]. A combined frequency and voltage control scheme was further proposed in [44] to result in improved energy saving profile. These open-loop frequency optimization schemes (OLFOS) result in optimal speed curves for different loads while maintaining a constant stroke frequency. Though well-performing in laboratory conditions, the OLFOS is difficult to implement in field conditions, due to a number of reasons: (i) the frequency is expressed in terms of optimized Fourier coefficients and typical frequency converters do not have adequate interfaces to receive them, (ii) the overall performance is strongly dependent on the accuracy of the complicated SRP model utilized and is highly sensitive to system parameters, (iii) they employ a genetic algorithm to find the optimum frequency, resulting in computation times much longer than those accommodated by the real-time on-field SRP and (iv) due to their open-loop nature, tracking changes in frequency from one cycle to the next is difficult. Consequently, to overcome these drawbacks of the OLFOS, this paper proposes a closed-loop frequency control scheme (CLFCS). The main advantages of the proposed method include: effective reduction of the peak magnitude of torque delivered within one stroke, robustness to sudden changes in operational parameters, easy tuning and overall simplicity.

The rest of the paper is organized as follows: Section 2 presents the full electromechanical model for the SRP, valid for real-time variable frequency operation. Section 3 describes the open-loop frequency optimization scheme (OLFOS) and presents details of its simulated performance. These results are employed to benchmark the proposed closed-loop scheme. Section 4 describes the proposed closed-loop frequency control scheme (CLFCS). Simulation results for the nominal closed-loop system are compared with those obtained by the open-loop scheme to clearly demonstrate the achieved performance improvement. The performance of the closed-loop scheme is then quantified under variations in the dynamic level of the liquid as well as for changing SPM, to demonstrate the scheme’s robustness over commonly encountered field conditions. In Section 5 we summarize the study and drawn main conclusions

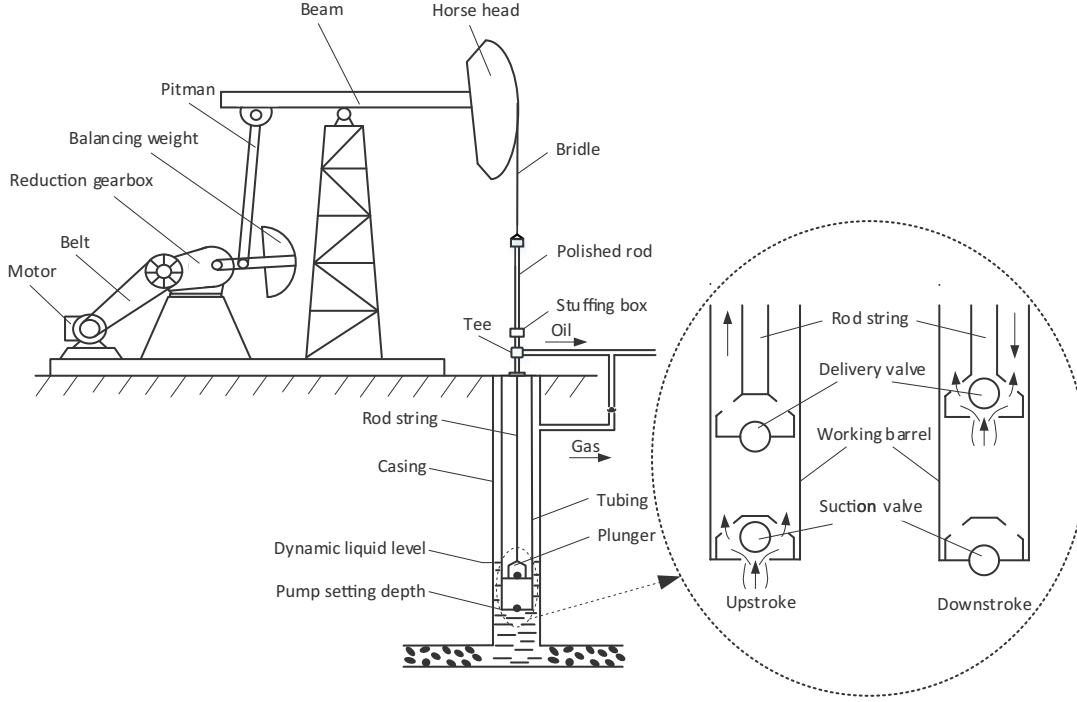


Figure 1: A schematic diagram of the sucker-rod pumping system (SRP). The rotational motion of the motor is converted into a reciprocating movement of the plunger through the surface and downhole transmission mechanism. Its one period is consisted of two operational regimes: (i) upstroke - when the fluid is absorbed into the barrel and (ii) downstroke - when the fluid is discharged out of the barrel.

from this work.

## 2. System modelling

A schematic diagram showing main components of an SRP how it operates is depicted in Fig. 1. In this system there are four sources generating dynamic interactions, namely, (i) the electric motor, (ii) the surface transmission mechanism, (iii) the longitudinal vibration of the rod-string and (iv) the reciprocating movement of the pump. To simulate the dynamics of the actual SRP system as accurately as possible, a coupled electromechanical model of the SRP actuated using a real-time variable frequency drive, is first formulated and validated using the field test data.

### 2.1. Surface transmission mechanism

The surface transmission mechanism is modelled as a single degree-of-freedom rigid system, where the crank mechanism is represented as an equivalent moment of inertia. The dynamics of this subsystem is described by the following equation [16, 45, 46]:

$$J_e \ddot{\theta}_c + \frac{1}{2} \dot{\theta}_c^2 \frac{dJ_e}{d\theta_c} = M_D - M_L, \quad (1)$$

where

$$M_L = \frac{L_R L_A}{L_C} \frac{\sin \alpha}{\sin \beta} (F_{RL} - F_b) \varepsilon_p - F_c L_R \sin \theta_c. \quad (2)$$

$M_D$  is the equivalent driving torque;  $M_L$  is the equivalent load torque;  $J_e$  is the system equivalent rotating inertia;  $\theta_c$  is the crank angle;  $F_{RL}$  is the polished rod load equalling the elastic strain at the top of rod string plus it's self-weight;  $F_b$  is the weight due to structural imbalance;  $F_c$  is the weight of the crank plus the counterweight;  $\varepsilon_p$  is the transmission efficiency of the four-bar linkage;  $L_R$  is the length of crank;  $L_C$  is the length of back beam;  $L_A$  is the length of front beam.

## 2.2. Electric motor

A SRP system is typically driven by a three-phase asynchronous motor. To simplify, the coupling of the motor inner variables, the  $dq$  two-phase synchronously rotating frame is employed [47, 48], and hence the dynamic model of the motor can be written as:

$$\begin{cases} M_m = \frac{n_p L_m}{L_r} (i_{sq} \psi_{rd} - i_{sd} \psi_{rq}), \\ \frac{d\psi_{rd}}{dt} = -\frac{R_r}{L_r} \psi_{rd} + (\omega_1 - \omega) \psi_{rq} + \frac{L_m R_r}{L_r} i_{sd}, \\ \frac{d\psi_{rq}}{dt} = -\frac{R_r}{L_r} \psi_{rq} - (\omega_1 - \omega) \psi_{rd} + \frac{L_m R_r}{L_r} i_{sq}, \\ \frac{di_{sd}}{dt} = \frac{L_m R_r}{\sigma L_s L_r^2} \psi_{rd} + \frac{L_m}{\sigma L_s L_r} \omega \psi_{rq} - \xi i_{sd} + \omega_1 i_{sq} + \frac{U_{sd}}{\sigma L_s}, \\ \frac{di_{sq}}{dt} = \frac{L_m R_r}{\sigma L_s L_r^2} \psi_{rq} - \frac{L_m}{\sigma L_s L_r} \omega \psi_{rd} - \xi i_{sq} - \omega_1 i_{sd} + \frac{U_{sq}}{\sigma L_s}, \end{cases} \quad (3)$$

where

$$\begin{cases} \xi = \frac{R_s L_r^2 + R_r L_m^2}{\sigma L_s L_r^2}, \\ \sigma = 1 - \frac{L_m^2}{L_s L_r}, \\ U_{ds} = (\frac{\sqrt{6}}{3} U_a - \frac{\sqrt{6}}{6} U_b - \frac{\sqrt{6}}{6} U_c) \cos(\int_0^t \omega_1 dt) + (\frac{\sqrt{2}}{2} U_b - \frac{\sqrt{2}}{2} U_c) \sin(\int_0^t \omega_1 dt), \\ U_{qs} = -(\frac{\sqrt{6}}{3} U_a - \frac{\sqrt{6}}{6} U_b - \frac{\sqrt{6}}{6} U_c) \sin(\int_0^t \omega_1 dt) + (\frac{\sqrt{2}}{2} U_b - \frac{\sqrt{2}}{2} U_c) \cos(\int_0^t \omega_1 dt), \\ \omega_1 = 2\pi f, \\ \omega = n_p \dot{\theta}_m. \end{cases} \quad (4)$$

$M_m$  is the motor driving torque ( $M_D = i_{mc} \varepsilon_{mc} M_m$ );  $i_{mc}$  and  $\varepsilon_{mc}$  are the transmission ratio and transmission efficiency between the motor and the crank;  $\psi_{rd}$  and  $\psi_{rq}$  denote the rotor flux along  $d$  and  $q$  axis respectively;  $i_{sd}$  and  $i_{sq}$  are the stator current along  $d$  and  $q$  axis respectively;  $R_s$  and  $R_r$  are

the resistances of stator and rotor respectively;  $L_s$ ,  $L_r$  and  $L_m$  are the self-inductance of stator, the self-inductance of rotor and the mutual inductance between the stator and rotor respectively;  $f$  is the motor driving frequency;  $n_p$  is the number of pole-pairs the motor possesses;  $\theta_m$  is the rotor angle of motor ( $\theta_m = i_{mc}\theta_c$ );  $U_a$ ,  $U_b$  and  $U_c$  are the three phase voltages respectively. Thus, the three phase-voltages can be written as:

$$U_i = U_m \sqrt{2} \sin(2\pi f t + \varphi_i), \quad (5)$$

where  $U_m$  is the effective value of the voltage and equals 220 V;  $i$  stands for the  $a$ ,  $b$  and  $c$  phases;  $\varphi_a$ ,  $\varphi_b$ ,  $\varphi_c$  is 0,  $-2/3\pi$ ,  $-4/3\pi$  respectively;  $k_f$  is the ratio coefficient, which has a value of  $f/50$  when the frequency is below 50 Hz and a value of 1 when the frequency is above 50 Hz. Since the frequency is adjusted in real-time and the constant V/F control principle is employed in this work, the general three-phase voltage equation given in (5) can be replaced with the one presented in (6) below.

$$U_i = U_m \sqrt{2} k_f \sin(2\pi \int_0^t f dt + \varphi_i). \quad (6)$$

Since the components of rotor current are given by:  $i_{rd} = \frac{1}{L_r}(\psi_{rd} - L_m i_{sd})$  and  $i_{rq} = \frac{1}{L_r}(\psi_{rq} - L_m i_{sq})$ , the copper loss in the motor can be calculated as:

$$P_{cus} = (i_{sd}^2 + i_{sq}^2)R_s + (i_{rd}^2 + i_{rq}^2)R_r. \quad (7)$$

### 2.3. Rod-string's longitudinal vibration

An oil-well is typically several kilometers deep and therefore a rod-string will generate longitudinal vibrations during its upward and downward motion. In this paper, the widely used Gibbs's wave equation is employed to model these dynamic effects, [7, 49, 50]. This approach assumes that the rod-string is linearly elastic with a polished rod displacement, and the pump load acting as excitation. Referring to its mechanical model described in Fig. 2, the equations describing the rod-string's longitudinal vibration can be written as follows

$$\begin{cases} \frac{\partial^2 u}{\partial t^2} - \frac{E_{rd}}{\rho_{rd}} \frac{\partial^2 u}{\partial x^2} + \frac{\mu}{\rho_{rd} A_{rd}} \frac{\partial u}{\partial t} = -\frac{d^2 u_a}{dt^2} - \frac{\mu}{\rho_{rd} A_{rd}} \frac{du_a}{dt}, \\ u(x, t) |_{x=0} = u_a, \\ E_{rd} A_{rd} \frac{\partial u(x, t)}{\partial x} |_{x=L_{rd}} = F_{PL}, \end{cases} \quad (8)$$

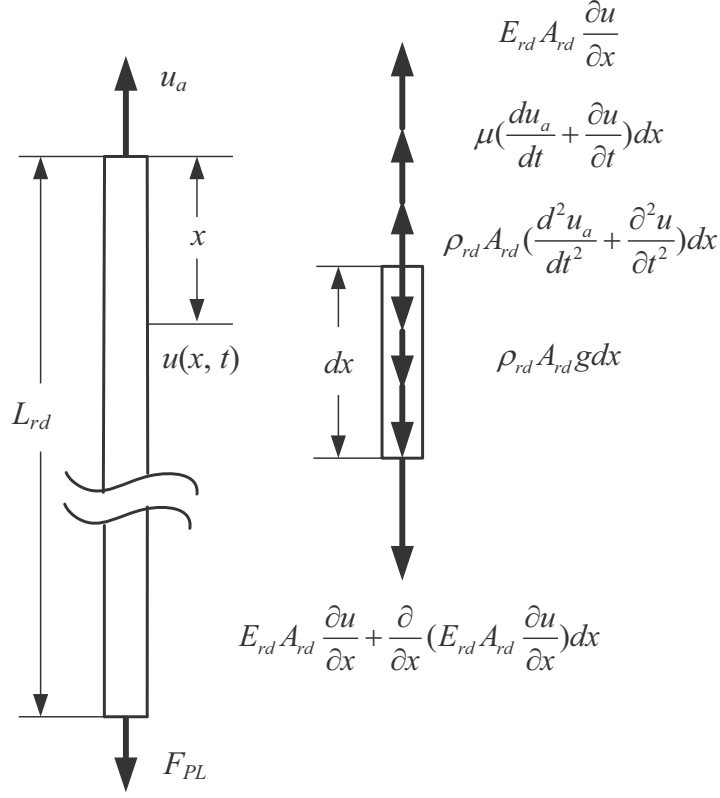


Figure 2: Longitudinal model of the rod string. The rod string is assumed as an elastic part whose arbitrary micro element suffers the axial force, the damping force, the inertial load and gravity, incorporating the excitations from the polished rod displacement and the pump load.

where  $u(x, t)$  is the displacement of the sucker rod at an arbitrary depth and time;  $u_a$  is the displacement expressed as a function of  $\theta$ , [46];  $\mu$  is the oil viscosity;  $L_{rd}$ ,  $E_{rd}$ ,  $A_{rd}$ ,  $\rho_{rd}$  are the length, elastic modulus, cross-sectional area and density of the rod-string respectively, and  $F_{PL}$  is the pump load as a result of the pressure difference between the upper and lower surfaces of plunger. Then,

$$F_{PL} = A_p(p_d - p) - A_{rd}p_d, \quad (9)$$

where  $A_p$  is the cross-sectional area of plunger,  $p_d$  is the pump outlet pressure and  $p$  is the pump pressure.

#### 2.4. Pump pressure transitions

During each cycle of operation, the pump pressure transitions into four distinct stages as shown schematically in Fig. 3 and explained below.

- *Stage 1:* Prior to the opening of the standing valve, the plunger moves up and the pump pressure decreases.

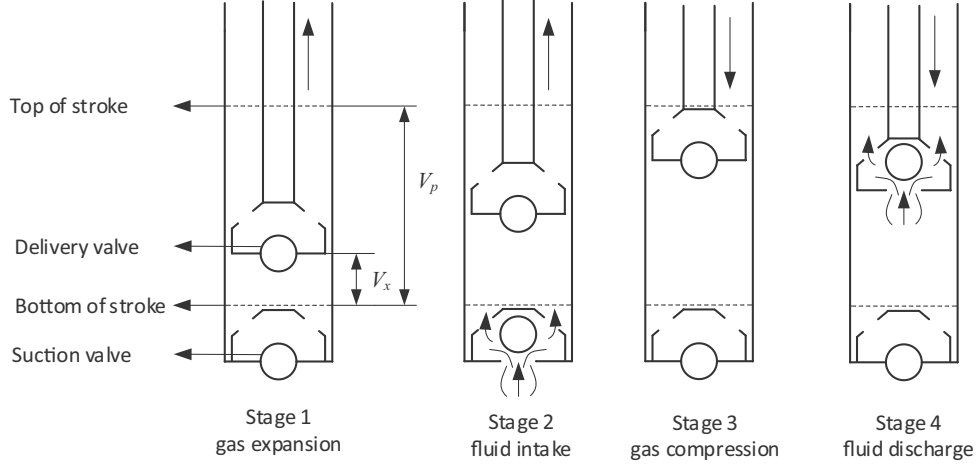


Figure 3: The four stages for each cycle of pump operation. Stage 1: Prior to the opening of the standing valve, the plunger moves up and the pump pressure decreases. Stage 2: Pump pressure reduces to the pump inlet pressure and the fluid is moved into the barrel. Stage 3: Plunger arrives at the top of the stroke as the standing valve is closed and pump pressure rises leading to plunger beginning its downward descent. Stage 4: Pump pressure increases to pump outlet pressure draining out the fluid.

- *Stage 2*: When the pump pressure reduces to the pump inlet pressure, the fluid is moved into the barrel and the pump pressure is maintained.
- *Stage 3*: As the plunger arrives at the top of stroke, the standing valve is closed and the pump pressure rises while the plunger begins its downstroke.
- *Stage 4*: Finally, as the pump pressure increases to pump outlet pressure, the fluid is drained out of the barrel and the pump pressure is brought back to the pump outlet pressure.

If it is assumed that an oil-well has sufficient fluid supply capacity then, the pump pressures for each of these four stages can be written as [46, 51]:

$$\begin{cases} p = \left( \frac{V_{og}}{V_{og} + V_x} \right)^n p_d, & \text{Stage 1 : } v_p > 0 \quad \text{and} \quad p > p_s \\ p = p_s, & \text{Stage 2 : } v_p > 0 \quad \text{and} \quad p = p_s \\ p = \left( \frac{V_g}{V_g - V_p + V_x} \right)^n p_s, & \text{Stage 3 : } v_p < 0 \quad \text{and} \quad p < p_d \\ p = p_d, & \text{Stage 4 : } v_p < 0 \quad \text{and} \quad p = p_d \end{cases} \quad (10)$$

where  $p_s$  is the pump inlet pressure,  $V_{og}$  is the gas volume in the pump when the plunger arrives at the bottom of the stroke,  $V_g$  is the gas volume in the pump when plunger arrives at the top of the stroke,  $V_x$  is the traveling volume when plunger displacement is  $x$ ,  $V_p$  is the pump stroke volume and  $n$  is the gas polytropic exponent and  $v_p$  is the velocity of the plunger.



### 2.5. Overall mathematical model

By combining Eq. (1) with Eq. (3), the mathematical model of surface system can be expressed as a set of Ordinary Differential Equations (ODEs) of the first order by Eq. (11). The rod-string longitudinal vibration defined by Eq. (8) and the pump pressure transitions by Eq. (10) can be rewritten in the form of Eqs (12) and (13), where more details can be found in [44]. Therefore, the overall mathematical model is established by combining with Eqs (11), (12) and (13), which contains fifteen state variables  $\mathbf{X} = [\psi_{rd}, \psi_{rq}, i_{sd}, i_{sq}, \theta, \omega, x_{11}, x_{12}, x_{21}, x_{22}, x_{31}, x_{32}, x_{41}, x_{42}, p]$ . The Runge-Kutta method is used to integrate the dynamical system with an automatic integration step and the solving flow chart is shown in Fig. 4.

$$\begin{pmatrix} \psi'_{rd} \\ \psi'_{rq} \\ i'_{sd} \\ i'_{sq} \\ \theta'_c \\ \omega'_c \end{pmatrix} = \begin{pmatrix} -\frac{R_r}{L_r} & (\omega_1 - \omega) & \frac{L_m R_r}{L_r} & 0 & 0 & 0 \\ -(\omega_1 - \omega) & -\frac{R_r}{L_r} & 0 & \frac{L_m R_r}{L_r} & 0 & 0 \\ \frac{L_m R_r}{\sigma L_s L_r^2} & \frac{L_m}{\sigma L_s L_r} \omega & -\xi & \omega_1 & 0 & 0 \\ -\frac{L_m}{\sigma L_s L_r} \omega & \frac{L_m R_r}{\sigma L_s L_r^2} & -\omega_1 & -\xi & 0 & 0 \\ 0 & 0 & 0 & 0 & 0 & 1 \\ 0 & 0 & 0 & 0 & 0 & -\frac{J_e'}{2J_e} \end{pmatrix} \begin{pmatrix} \psi_{rd} \\ \psi_{rq} \\ i_{sd} \\ i_{sq} \\ \theta_c \\ \omega_c \end{pmatrix} + \begin{pmatrix} 0 \\ 0 \\ \frac{U_{sd}}{\sigma L_s} \\ \frac{U_{sq}}{\sigma L_s} \\ 0 \\ \frac{M_D - M_L}{J_e} \end{pmatrix}, \quad (11)$$

$$\begin{aligned} x'_{11} &= x_{12}, \\ x'_{12} &= -\frac{E_{rd}}{\rho_{rd}} \left( \frac{\pi}{2L_{rd}} \right)^2 x_{11} - \mu_* x_{12} + (u''_a + \frac{\mu}{\rho_{rd} A_{rd}} u'_a) \frac{2\alpha}{\pi} + F_{PL} \sqrt{\frac{2}{A_{rd} \rho_{rd} L_{rd}}} \sin\left(\frac{\pi}{2}\right), \\ x'_{21} &= x_{22}, \\ x'_{22} &= -\frac{E_{rd}}{\rho_{rd}} \left( \frac{3\pi}{2L_{rd}} \right)^2 x_{21} - \mu_* x_{22} + (u''_a + \frac{\mu}{\rho_{rd} A_{rd}} u'_a) \frac{2\alpha}{3\pi} + F_{PL} \sqrt{\frac{2}{A_{rd} \rho_{rd} L_{rd}}} \sin\left(\frac{3\pi}{2}\right), \\ x'_{31} &= x_{32}, \\ x'_{32} &= -\frac{E_{rd}}{\rho_{rd}} \left( \frac{5\pi}{2L_{rd}} \right)^2 x_{31} - \mu_* x_{32} + (u''_a + \frac{\mu}{\rho_{rd} A_{rd}} u'_a) \frac{2\alpha}{5\pi} + F_{PL} \sqrt{\frac{2}{A_{rd} \rho_{rd} L_{rd}}} \sin\left(\frac{5\pi}{2}\right), \\ x'_{41} &= x_{42}, \\ x'_{42} &= -\frac{E_{rd}}{\rho_{rd}} \left( \frac{7\pi}{2L_{rd}} \right)^2 x_{41} - \mu_* x_{42} + (u''_a + \frac{\mu}{\rho_{rd} A_{rd}} u'_a) \frac{2\alpha}{7\pi} + F_{PL} \sqrt{\frac{2}{A_{rd} \rho_{rd} L_{rd}}} \sin\left(\frac{7\pi}{2}\right), \end{aligned} \quad (12)$$

$$p' = \begin{cases} \frac{v_p A_p p_d}{V_{og}(-1/n)(p/p_d)^{-\frac{1}{n}-1}}, & \text{Stage 1 : } v_p > 0 \text{ and } p > p_s \\ 0, & \text{Stage 2 : } v_p > 0 \text{ and } p = p_s \\ \frac{v_p A_p p_s}{V_g(-1/n)(p/p_s)^{-\frac{1}{n}-1}}, & \text{Stage 3 : } v_p < 0 \text{ and } p < p_d \\ 0, & \text{Stage 4 : } v_p < 0 \text{ and } p = p_d \end{cases} \quad (13)$$

where  $\omega_c$  is the initial angular velocity of the crank,  $x_{i1}$  is the  $i$ -th modal coordinate of rod string longitudinal vibration ( $i=1,2,3,4$ ),  $\mu_* = \frac{\mu}{\rho_{rd}A_{rd}}$  and  $\alpha = \sqrt{2A_{rd}\rho_{rd}L_{rd}}$ .

### 3. Open-loop frequency optimization scheme

As elaborated earlier, it is beneficial to smoothen the load torque characteristics in the SRP system and this section describes an open-loop frequency optimization scheme to achieve this aim. As the instantaneous motor output power (MOP) is a good indicator of the load, the standard deviation of MOP,  $P_{std}$ , is chosen as the candidate function to be minimized.

#### 3.1. Design principle of open-loop control

As the SRP has a periodic operation where its period is decided by the power frequency, the variable frequency curve can be represented using a Fourier series

$$f(t) = f_b + \sum_{n=1}^N [a_n \cos(2\pi f_s n t) + b_n \sin(2\pi f_s n t)], \quad (14)$$

where the  $f_s$  is the SPM,  $f_b$  is the base frequency and  $(a_n, b_n)$  are the designed optimal Fourier coefficients.

To ensure that the required frequency curve is realized within acceptable accuracy, the first three harmonics of the fundamental are included. Thus,  $N = 3$ . To maintain a constant SPM, the average angular velocity of the motor is fixed for each cycle. As a motor typically employed in the SRP system is of the low-slip type, the variation in its slip-speed ratio can be ignored. Therefore, its angular velocity is decided by the power frequency, and the SPM can be kept unchanged if the average value of frequency in one period is constant before, and after controlling the frequency. With the average value of the sine and cosine terms in (14) are all 0, it can be concluded that the SPM remains unchanged as long as  $f_b$  equals the typical supply frequency, 50 Hz.

Typical operational limits imposed on the system are as follows:

$$\begin{cases} 20 \leq f(t) \leq 80, \\ F_{RL} - \max(F_{RL}) \leq 0, \\ M_m - \max(M_m) \leq 0, \end{cases} \quad (15)$$

where  $\max(F_{RL})$  is the maximum allowable polished rod load and  $\max(M_m)$  is the maximum allowable motor torque. Based on this, the optimization problem can be reformulated as a cost function minimization problem,

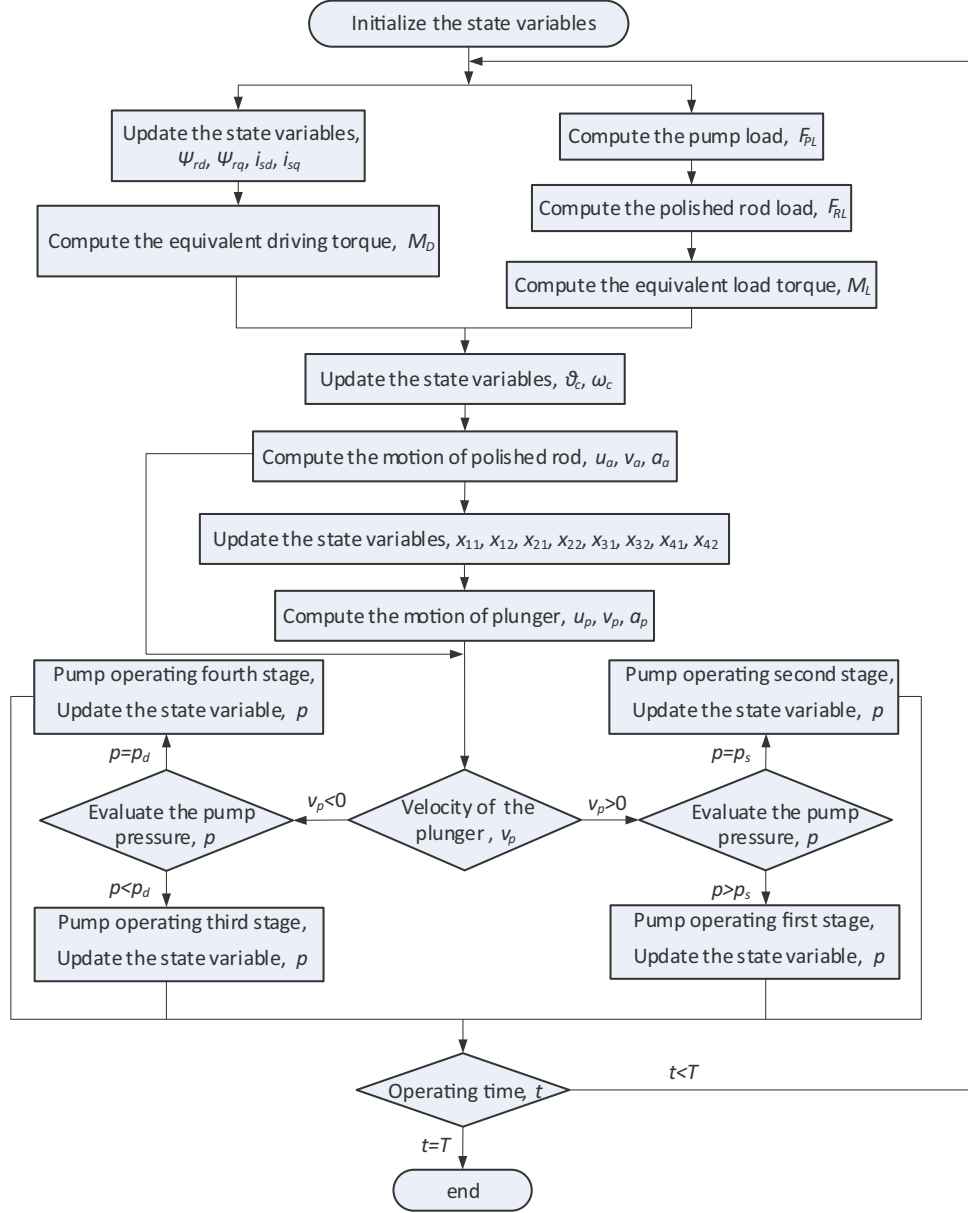


Figure 4: Computing flow chart for the numerical integration of the differential equations describing the overall mathematical model of the sucker-rod pumping system (SRP). The state variables are updated and all necessary auxiliary variables and parameters are calculated when solving the models describing dynamics of electric motor, surface transmission, rod string longitudinal vibration and pump pressure transitions and the iterative process terminates when the set simulation time  $t = T$  is reached.

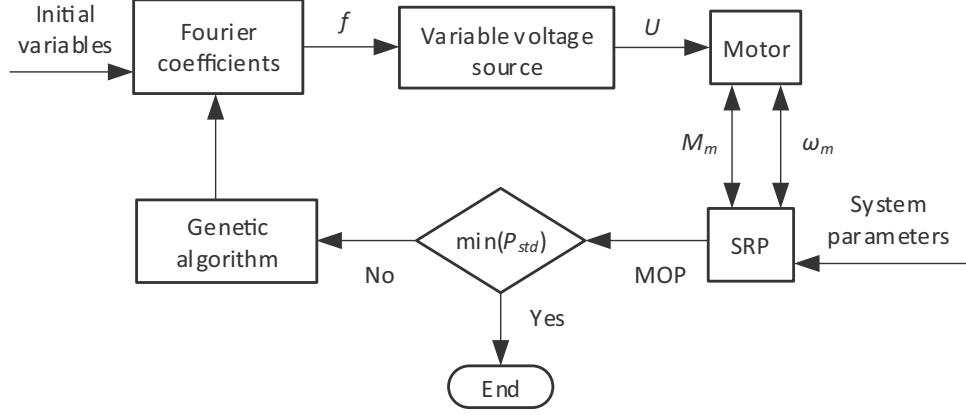


Figure 5: Flow chart for the proposed open-loop frequency optimization scheme (OLFOS). The OLFOS uses system parameters as inputs and employs a genetic algorithm to generate optimized Fourier coefficients used for expressing the supply frequency that minimizes the  $P_{std}$ .

Table 1: Field parameters of the oil-well number X2-322 from the Changqing Oilfield.

Well	X2-322	Stroke length	3 m
SPM	$6 \text{ min}^{-1}$	Pump diameter	57 mm
Pump setting depth	1200 m	Rod string diameter	22 mm
Rod string length	1200 m	Balancing weight	43.12 kN
Reservoir midpoint	1600 m	Oil density	$850 \text{ kg/m}^3$
Water content	97.4 %	Dynamic liquid level	1100 m
Casing pressure	0.3 MPa	Oil pressure	0.6 MPa
Fluid viscosity	0.086 Pa·s	Gas oil ratio	$60 \text{ m}^3/\text{m}^3$

$$\phi(x) = \min(P_{std}(f_b, a_1, b_1, a_2, b_2, a_3, b_3)), \quad (16)$$

where a genetic algorithm is applied to identify the Fourier coefficients that minimize  $P_{std}$  and a flow-chart for this scheme is shown in Fig. 5.

### 3.2. Open-loop results and discussion

Two cases were simulated and for the first case, the motor is supplied with an A.C. voltage at constant frequency (CFS). The second case is where the motor is controlled via the proposed OLFOS. For both cases, the motor torque as well as the MOP were recorded for one full period of the SRP. In order to make the simulations as realistic as possible, parameters recorded from the oil-well number X2-322 of the Changqing Oilfield were used to populate the established electromechanical model employed consequently to test the efficacy of the control schemes proposed herewith. These parameters are listed in Table. 1. The used SRP type is CYJ10-3-53HB and its basic parameters are listed in Table. 2, which is driven by a YE2-250M-6 motor and its parameters are listed in Table. 3. Based on the simulated results presented in Fig. 6, the following conclusions can be drawn:

Table 2: Typical mechanical parameters of sucker-rod pumping system.

Length of crank	1.03 m	Length of pitman	3.03 m
Length of beam back	2.82 m	Length of beam front	3.94 m
Length of frame	4.34 m	Weight of crank	9.80 kN
Weight of pitman	4.90 kN	Weight of beam	14.70 kN
Weight of balancing weight	49.98 kN	Weight of structure unbalance	2.5 kN
Transmission ratio of reduction gearbox	35	Transmission ratio of belt	4.67
Moment of inertia of small belt pulley	0.50 kg·m <sup>2</sup>	Moment of inertia of big belt pulley	2.00 kg·m <sup>2</sup>
Moment of inertia of gearbox	2.25 kg·m <sup>2</sup>		

Table 3: Typical electrical parameters of a motor used in sucker-rod pumping systems

Rated power	37 kW	Rated speed	980 rpm
Rotor rotary inertia	0.834 kg·m <sup>2</sup>	Stator resistance	0.082 $\Omega$
Rotor resistance	0.050 $\Omega$	Stator self-inductance	0.02783 H
Rotor self-inductance	0.02783 H	Mutual inductance	0.02711 H

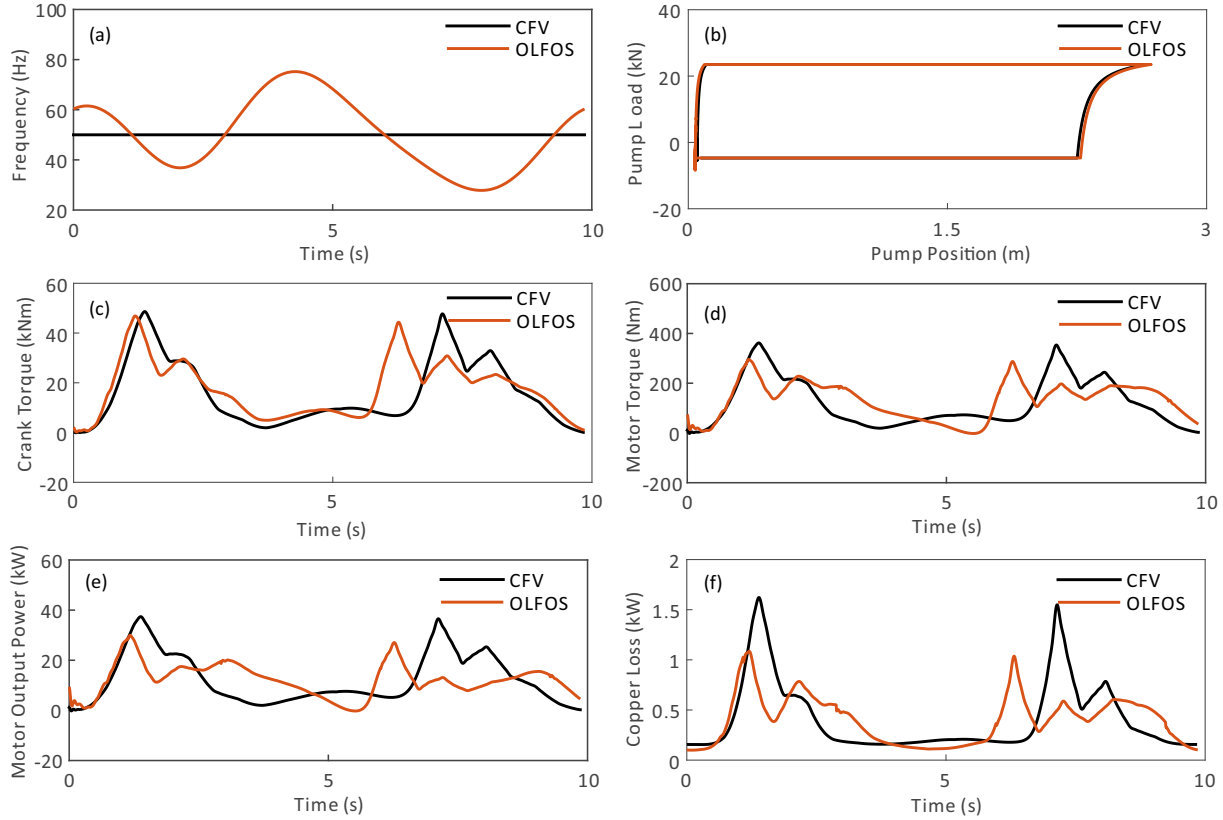


Figure 6: Frequency, torque and MOP time histories for both CFS and OLFOS driven SRP. (a) The evolution of frequency vs time. In the CFS, the supply voltage frequency is kept constant, while in the OLFOS, the frequency undergoes a ‘double hump’ transition within one stroke period. (b) Plot of pump load vs pump position. The enclosed area is indicative of the effective pump power and consequently, production. (c) Crank torque plotted against time clearly showing the double-hump nature of the load. (d) Time history of the motor torque for one period. The OLFOS case clearly shows the “peak shaving and valley filling” effect. (e) MOP vs CFV showing that the OLFOS approach reduces the peak MOP and consequently the variation between the minimum and maximum MOP values. (f) Copper loss ( $I^2R$ ) shows reduced peaks for the OLFOS case, as a consequence of lower current ( $I$ ).

- A downhole pump card is employed to record the position of the plunger and the corresponding pump load for one period. These two quantities, when plotted against each other, ascribe a closed area, see Fig. 6(b). This closed area is equivalent to the work done by the pump, and is a good estimate of the pump’s effective power for one period, [52–54]. As can be seen from Fig. 6(b), this closed area remains unchanged for the CFS as well as the proposed OLFOS. This indicates that the variable driving frequency utilized in the proposed OLFOS maintains the average effective power of the pump unchanged with respect to the standard CFS for any given SPM pump rate.
- The average MOP generally serves as a good indicator of the power consumed by the mechanical load. As a result, the MOP curves for the traditionally employed CFS and proposed OLFOS are plotted for one period in Fig. 6(e). Computing the average MOP in both cases results in the same value showing that the power consumed by the mechanical load remains unchanged irrespective of the supply voltage frequency profile (constant or variable).
- As shown in Fig. 6(d), compared to the CFS, the proposed OLFOS exhibits a decrease in the standard deviation of motor driving torque by 23.48% (from 96.47 Nm to 73.82 Nm). Additionally, the peak value of the motor driving torque is reduced by 18.25% (from 361.84 Nm to 295.79 Nm). This reduction in load fluctuation can potentially prolong the operating life of the SRP system. However, the fluctuation of crank torque is reduced only slightly as shown in Fig. 6(c). Therefore, this desirable “peak shaving and valley filling” effect is mainly due to the redistribution of the inertial load from motor to crank, brought about by optimizing the power frequency in one cycle.
- The  $P_{std}$  is decreased by 35.74% (from 9.99 kW to 6.42 kW) and the peak value of MOP is reduced by 19.98% (from 37.39 kW to 29.92 kW), as shown in Fig. 6(e). This can potentially facilitate the adoption of a motor of a significantly lower rating; thereby reducing capital costs and increasing motor efficiency.
- The reduced fluctuation in copper losses, as shown in Fig. 6(f) indicates the reduction in the peak value of the current, a beneficial outcome. The energy saving due to reduced copper losses is approximately 7% (from 0.41 kW to 0.38 kW). Though not significant as a stand-alone, when taken in context of a typical oil-field that employs tens or even hundreds of these SRP systems, the energy saving is significant.

It is well-known that for almost all systems with varying system parameters, operating conditions and targets, a well-designed closed-loop control scheme tends to outperform open-loop counterparts. With

this motivation, the next section presents the formulation and analysis of a closed-loop frequency control scheme for the SRP, to deliver further improvement in its load profile.

#### 4. Closed-loop frequency control scheme

The main motivation of the closed-loop frequency control scheme (CLFCS) proposed herewith is to overcome the drawbacks of the open-loop frequency optimization scheme described earlier. The proposed closed-loop control scheme uses the MOP data to modify the supply voltage frequency such that the peak MOP as well as its  $P_{std}$  is reduced, thereby allowing the use of a motor of smaller rating to supply the SRP load.

##### 4.1. Design principle of closed-loop control

Based on the open-loop simulations presented in Section 3, the average MOP remains constant, irrespective of the instantaneous frequency changes and consequently the motor speed. In turn, when there is no variation in the external factors, the SPM can be guaranteed to remain unchanged if the real-time frequency is adjusted for a constant average MOP value. Moreover, in order to minimize load variations for the smallest motor rating, a constant average MOP must be maintained. Hence the driving frequency, the MOP and its average value are taken as the control, feedback and reference inputs respectively. To maintain control accuracy, the average value is recalculated at the end of each subsequent period. A SIMULINK block-diagram of the proposed control scheme is shown in Fig. 7, where the frequency control block provides control signal to the SRP block whose output is taken as the feedback signal and transmitted to the MOP average block to get the reference signal. This work focuses on improving the overall performance of a mature and relatively simple electromechanical system namely, a sucker-rod pump employed to provide artificial lift in onshore oilwells. Hence, an overly complex or computationally expensive technique would not convince users to adopt the improvement-driven control strategy proposed herewith. Moreover, complicated control parameter tuning schemes also lend themselves to several search-related infinite-loops resulting in deeming the overall scheme unimplementable. As a consequence, a simple integrator-based tracking loop is incorporated in this control scheme.

As the system is nonlinear, a simple theoretical stability proof is difficult. Furthermore, as this is a practical system, a thorough investigation of system stability over a range of control gain is more useful compared to a formal stability proof. To ensure that gain selection was based on the steady-state response of the system and not its transient response, the second period of the closed-loop SRP system

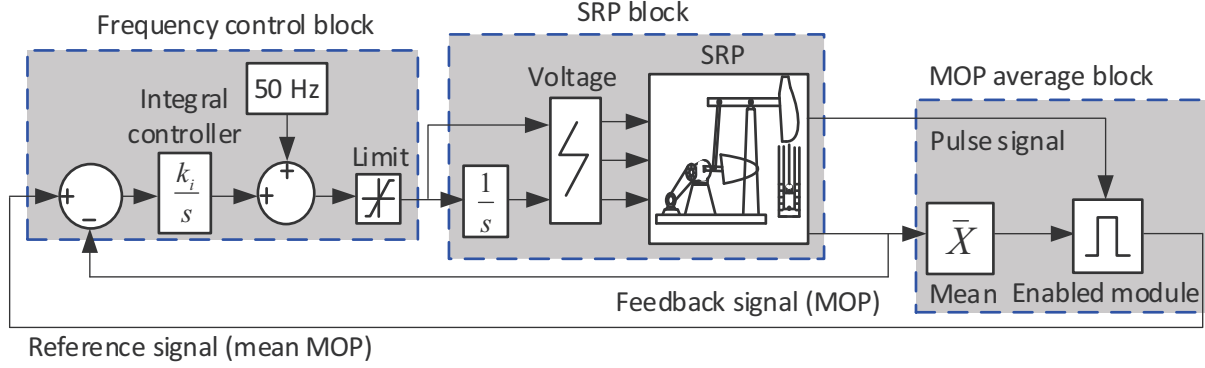


Figure 7: Representative block diagram for the proposed CLFCS. The supply frequency and its integral are used as inputs for the voltage supply module. The voltage supply module supplies voltage to the SRP motor with the appropriate magnitude and frequency. The mean value of the MOP for one cycle is computed and used as the reference signal while the instantaneous value of MOP is used as the feedback.

was analyzed for a range of control gains. The plot of the achieved  $P_{std}$  vs control gain is shown in Fig. 8 for the gain within  $[0.001, 0.02]$ , using a resolution of 0.001 for each incremental gain point. As seen from the plot, increasing the control gain gradually reduces the standard deviation of the MOP till the controller gain reaches 0.01. Beyond this point the standard deviation of MOP increases rapidly and higher gains result in chattering. Increasing the gains further will result in instability. Consequently, a control gain of 0.01 was used for all simulations presented herewith.

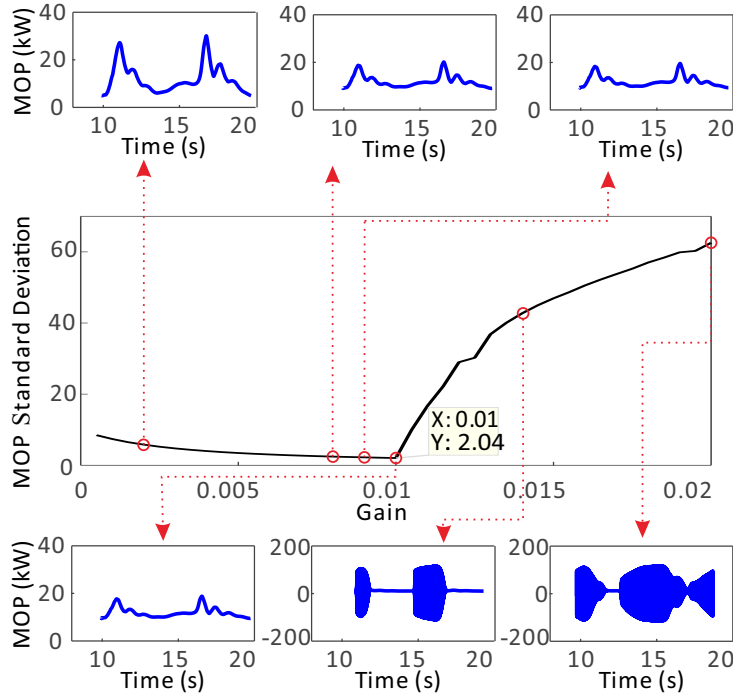


Figure 8: Standard Deviation of MOP ( $P_{std}$ ) vs Control gain for the interval  $[0.001, 0.02]$ . Along with the increase of control gain, the  $P_{std}$  is first decreasing and then increasing, with the minimum occurring at a gain value of 0.01. Inserts show plots of the second period of the closed-loop instantaneous power vs time.  $P_{std}$  increases and leads to chattering, once the gain value exceeds 0.01.



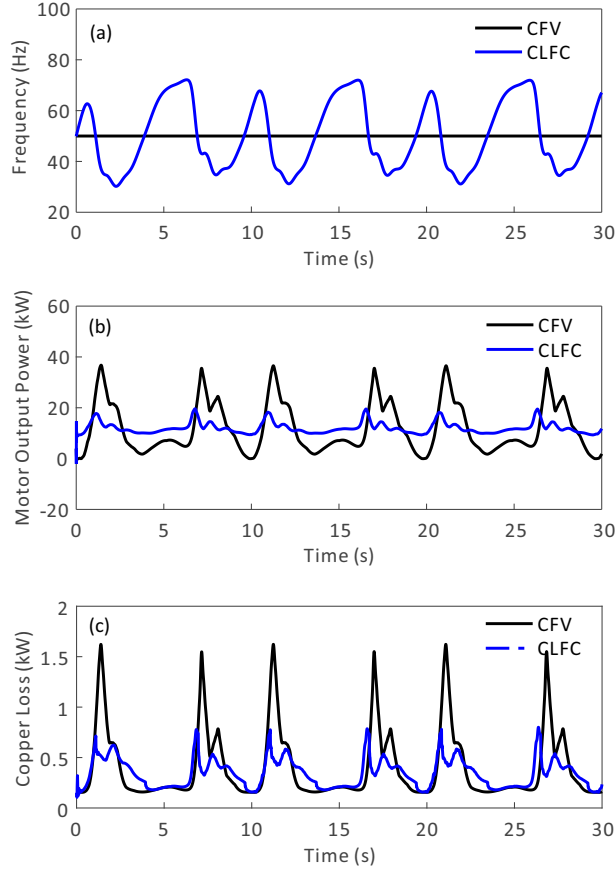


Figure 9: Performance of the proposed CLFCS approach against the traditional CFS. (a) The evolution of frequency over time shows that unlike the CFS, the CLFCS provides a variable frequency supply to adapt to the load variation. (b) MOP depicts that the CLFCS effectively reduces the load fluctuation and reaches steady quickly (within the first stroke period). (c) A plot of copper loss over one period shows that the peaks are effectively reduced.

#### 4.2. Closed-loop results and discussion

An oil-well undergoes parameter changes (such as changes in the oil level) throughout its production lifetime. Based on these changes, three broad operating regimes can be identified: (i) nominal operation, where parameters of the oil-well remain unchanged, (ii) changes in liquid level where the level of the liquid within the well undergoes dynamic variation and (iii) changes in the rate of production, which can be adjusted by altering the SPM accordingly. In this section, the parameters of the same oil-well, number X2-322 from the Changqing Oilfield, as reported in Table 1, are used to test the efficacy of the proposed closed-loop control strategy for the three regimes discussed earlier. All the simulations are performed by setting the integral control gain to 0.01, the selection process of which has been described in the last paragraph of Subsection 4.1. Though this may seem like a very low value, this is mainly due to the large internal gain that the system imparts to the output when compared with the input.

As mentioned earlier, in this regime, the oil-well parameters remain unchanged. This is the simplest

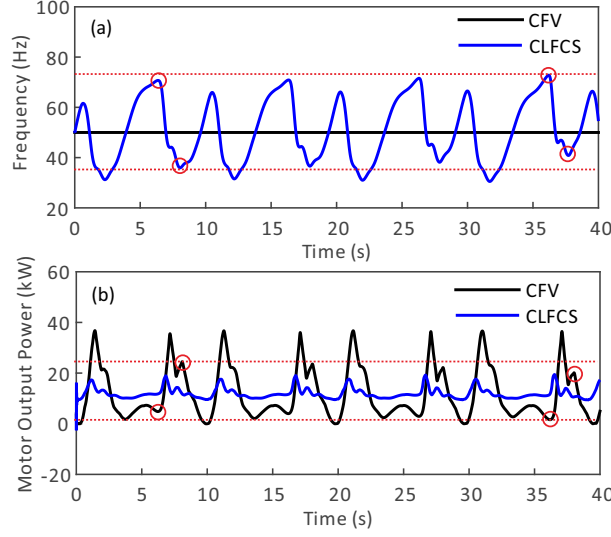


Figure 10: Comparison of the CFS and CLFCS driven SRP performance in the presence of variations in liquid level. (a) Frequency provided by CLFCS varies with the decrease in liquid level to adapt the load variation caused by it. (b) MOP evolutions shows that with the decrease in liquid level depth, the proposed CLFCS outperforms the traditional CFS in terms of reduced fluctuations in MOP and better balance.

scenario that the proposed CLFCS faces. Plots for frequency as well as MOP for the traditional CFS as well as the proposed CLFCS, are presented in Fig. 9. As seen from Fig. 9(a), the proposed control scheme varies the supply frequency depending on the instantaneous load, as opposed to the CFS which maintains a fixed frequency. To analyze and quantify the steady-state behaviour of the proposed control scheme, the second period after engaging the closed-loop control scheme is used for comparison. Results show a reduction in  $P_{std}$  by 79.58% (from 9.99 kW to 2.04 kW), in peak MOP by 47.66% (from 37.39 kW to 19.57 kW) and in average copper losses by 21.95% (from 0.41 kW to 0.32 kW) when compared with the CFS method. Moreover, when compared with the earlier proposed open-loop frequency optimization scheme (OLFOS), the proposed CLFCS shows a reduction in  $P_{std}$  by 43.84% and in peak MOP by 27.68%, see Fig. 6. This clearly demonstrates a superior performance delivered by the proposed closed-loop scheme. It can be concluded that under nominal conditions, the proposed CLFCS enables a motor of significantly lower rating to be incorporated to supply the SRP load adequately. Moreover, due to the smoothing of the load characteristics, the lower-rated motor will operate at close to its full-load capacity, thereby improving its operational efficiency.

It is known that over the period of its production life, the liquid level in the oil-well will gradually drop. This reduction is slow enough to assume that the liquid level in the oil-well is static for most control applications. However, the liquid level could drop by 100 m in ten minutes if the swabbing parameters do not sync with the formation fluid supply [45]. To test the robustness limits of the employed control scheme, we selected an extreme (worst) case where the liquid level drops by 20 m after every lift cycle.

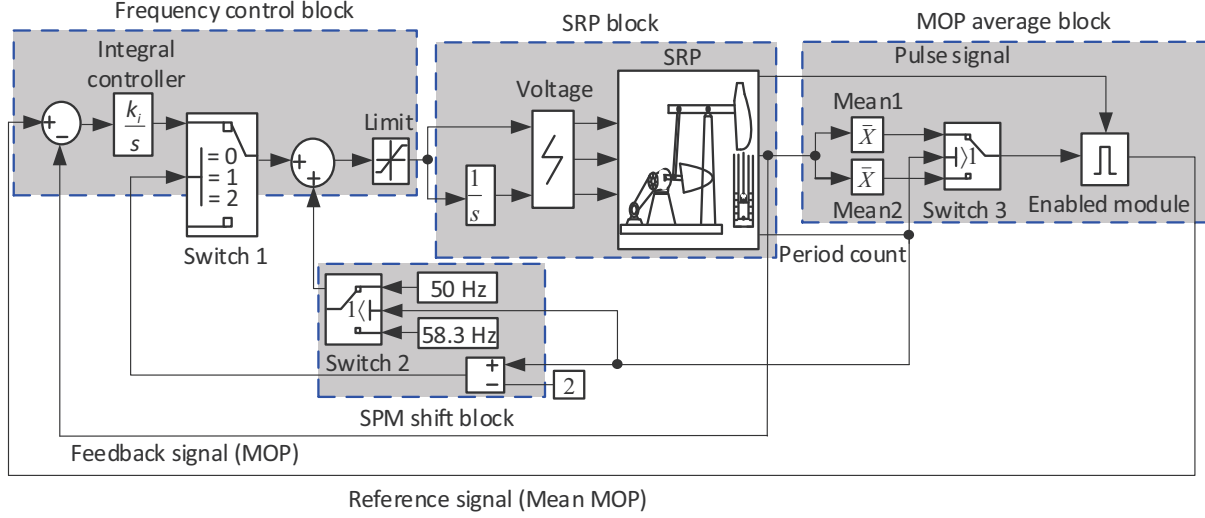


Figure 11: CLFCS block diagram for the variable SPM case. The number of completed SRP stroke periods are counted in order to switch the controller on and off after changing the SPM. After the first period, the period counter increments by one and switches 1, 2 and 3 are connected such that the controller is out of work. The SPM is adjusted from  $6 \text{ min}^{-1}$  to  $7 \text{ min}^{-1}$  and the corresponding calculation period for MOP is changed. Then, the switch 1 is re-engaged and the controller goes back to work after the period count is five.

Computed time histories for supply frequency and MOP for the CFS as well as the proposed CLFCS are presented in Fig. 10. It can be seen that the load balance worsens with declining liquid level. However, the proposed CLFCS can adjust the frequency in time and is still able to maintain an acceptable load balance.

The operator generally changes the SPM to satisfy the production requirements. These adjustments are made gradually, depending on its significant effect on production and load [22, 55]. To further test the robustness of the proposed control scheme in the presence of this type of uncertainty or disturbance, the SPM is incrementally varied by 1 unit from its nominal value of  $6 \text{ min}^{-1}$ . Again, this variation and its instantaneous change was considered to simulate a notional upper limit of what is typically observed in oil fields. This is achieved by changing the supply frequency from 50 Hz to 58.3 Hz and is effected after the completion of the second SRP stroke. The control block diagram for this case is given in Fig. 11. Plots for supply frequency and MOP are presented in Fig. 12. It can be seen that changing SPM results in significant changing in peak MOP values when the SRP is operating without the CLFCS engaged. On the other hand, the proposed control scheme can still reach steady-state relatively quickly ( $t=54.11 \text{ s}$ ), see Fig. 12. Moreover, the peak MOP value is reduced from 47.09 kW to 22.78 kW, demonstrating that the proposed CLFCS is robust to changes in SPM.

There are more than 2 million oil-wells around the world where nearly 50% are operating with artificial lifting equipment [5]. More than 70% of these systems are SRP and the rest are using progressive cavity

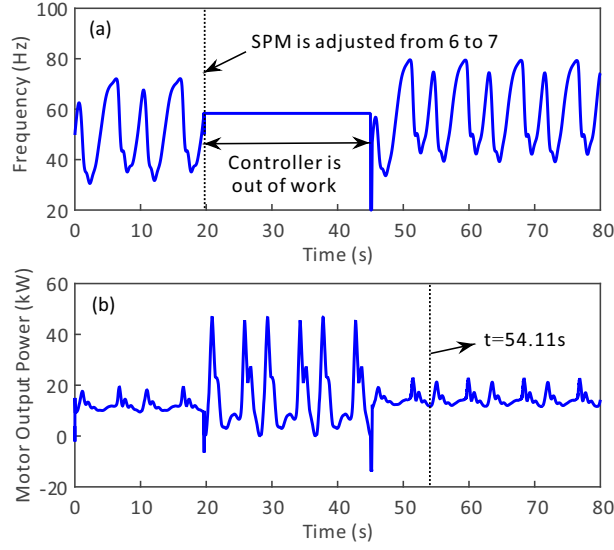


Figure 12: Dynamic responses when SPM is adjusted from  $6 \text{ min}^{-1}$  to  $7 \text{ min}^{-1}$ . (a) The time history of frequency indicates that the average frequency for one period changes from 50 Hz to 58.3 Hz. The controller stops three periods after the change in SPM to  $7 \text{ min}^{-1}$ , in order to accurately calculate the average MOP. (b) MOP shows that the controller performs excellently and reaches steady-state within one stroke period. An effective reduction in the peak MOP is also observed.

pumps, electric submersible pumps and gas lift [6, 7]. With the cost of electronics decreasing and the need for automated systems, more oil-wells are equipped with frequency conversion control cabinet to adjust SPM automatically against oil production or pump fullness [1, 38, 40]. Therefore, the CLFCS can reduce motor rating and motor inner loss of SRP without a significant investment for new equipment. Taking a particular oil-well discussed in this paper as an example, evaluated economic benefits brought by CLFCS globally are obtained by:

(i) Reducing motor rating. The original motor type YE2-250M-6 with 37 kW power rating and costing around \$915 can be replaced by YE2-200M-6 with 22 kW power rating and costing \$565. Here the motor rating is reduced by 47%, and consequently \$245M can be saved.

(ii) Reducing motor inner loss. The motor copper losses can be reduced by 0.09 kW each period, which results in approximately \$40M will savings per year assuming electricity cost of \$0.07 per kilowatt hour.

To further demonstrate the advantages of using CLFCS, additional comparisons have been made and Table. 4 shows reductions in motor rating, copper loss and standard deviation of the motor output power for four additional oil wells within the Changqing Oilfield. The results are consistent with the previous conclusions that CLFCS is capable of significantly reducing the motor rating within 42.21%-54.45%, the copper loss within 17.93%-28.37% and the load variation within 75.76%-85.83%.

Table 4: Results comaprison under the closed-cloop frequency control scheme

	W41-2	Y52-22	F45-52	C83-14
Motor rating reduction (%)	54.45	42.21	50.77	46.69
Copper loss reduction (%)	28.37	17.93	24.92	20.68
Reduction on standard deviation of motor output power (%)	85.83	75.76	83.14	78.55

## 5. Closing remarks

In this work we have postulated that Energy Industry can make significant savings by reducing electric motors ratings of the popular SRP systems. We have shown by a field test data calibrated mathematical modelling and analysis that this can be achieved by application of robust controllers, which are fully integrated with the SRP systems. Here we have developed, modelled and analysed such integrated systems, specifically by examining two control schemes with open- and closed-loop controllers. The open loop scheme employs a genetic algorithm optimizing frequency in order to minimize fluctuations in a motor output power. Based on the load variation analysis of the sucker-rod pumping system (SRP), it is shown that the standard deviation of the motor output power  $P_{std}$  is a good measure of overall performance efficiency and load balance. It is further shown that minimizing  $P_{std}$  results not only in good balance and motor efficiency but also in the reduction of the required power rating of the motor supplying the SRP load.

As motor power is controlled using a variable frequency drive, an open-loop frequency optimizing scheme was formulated and analyzed. The scheme delivers promising results in reducing both the peak power as well as  $P_{std}$ . The genetic algorithm employed was computationally expensive and the scheme lacked robustness to any parameter variations.

Motivated by these results, a simple closed-loop control scheme was formulated and validated via simulations. The mean value of motor output power (MOP) for one full cycle was used as a reference and the instantaneous MOP was used as a feedback signal to generate the control signal (frequency of the motor supply voltage). The optimal control gain was chosen using a numerical search to ensure both performance and stability. The proposed closed-loop control scheme delivered stable, robust performance under nominal constant operating conditions as well as under changes in the liquid level and SPM values, and it also brings considerable economic benefit by reducing motor rating and motor inner loss.

Future work will include designing a gain optimization module that can deliver the best gain for different system parameters and external conditions. Experimental validations via implementation on an in-field SRP will also be pursued.

## Acknowledgments

The research in this paper is supported and funded by programs with China Scholarship Council (Grant 201708130108), and National Natural Science Foundation of China (Grant 51974276).

## Declarations of interest

There is no conflict of interest for all contributing authors.

## References

- [1] H. Q. Lv, J. Liu, J. Q. Han, A. Jiang, An energy saving system for a beam pumping unit, *Sensors* 16 (5) (2016) 1–13.
- [2] T. Aliev, A. Rzaev, G. Guluyev, T. Alizada, N. Rzaeva, Robust technology and system for management of sucker rod pumping units in oil wells, *Mechanical Systems and Signal Processing* 99 (15) (2018) 47–56.
- [3] J. Zhu, H.-Q. Zhang, Mechanistic modeling and numerical simulation of in-situ gas void fraction inside esp impeller, *Journal of Natural Gas Science and Engineering* 36 (2016) 144–154.
- [4] G. A. Moreno, A. E. Garriz, Sucker rod string dynamics in deviated wells, *Journal of Petroleum Science and Engineering* 184 (2020) 106534.
- [5] G. Takacs, *Electrical submersible pumps manual: design, operations, and maintenance*, Gulf professional publishing, 2018.
- [6] M. K. Dave, M. Ghareeb Mustafa, et al., Performance evaluations of the different sucker rod artificial lift systems, in: *SPE Symposium: Production Enhancement and Cost Optimisation*, Society of Petroleum Engineers, 2017.
- [7] M. M. Xing, S. M. Dong, A new simulation model for a beam-pumping system applied in energy saving and resource-consumption reduction, *SPE Production & Operations* 30 (2) (2015) 130–140.
- [8] Z. Wang, Y. Xu, Review on application of the recent new high-power ultrasonic transducers in enhanced oil recovery field in china, *Energy* 89 (2015) 259–267.
- [9] Y. Zhao, Y. Zhang, X. Lei, Y. Zhang, Y. Song, Co2 flooding enhanced oil recovery evaluated using magnetic resonance imaging technique, *Energy* 203 (2020) 117878.

- [10] X. Zhang, H. Che, Reducing heat loss of fluids in heavy oil wellbore using two-phase closed thermosyphon sucker rod, *Energy* 57 (2013) 352–358.
- [11] L. Cheng, H. Liu, S. Huang, K. Wu, X. Chen, D. Wang, H. Xiong, Environmental and economic benefits of solvent-assisted steam-gravity drainage for bitumen through horizontal well: A comprehensive modeling analysis, *Energy* 164 (2018) 418–431.
- [12] O. Ashrafi, P. Navarri, R. Hughes, D. Lu, Heat recovery optimization in a steam-assisted gravity drainage (sagd) plant, *Energy* 111 (2016) 981–990.
- [13] D. Baghernezhad, M. Siavashi, A. Nakhaee, Optimal scenario design of steam-assisted gravity drainage to enhance oil recovery with temperature and rate control, *Energy* 166 (2019) 610–623.
- [14] B. Y. Zheng, X. W. Gao, P. Rong, Sucker rod pump working state diagnosis using motor data and hidden conditional random fields, *IEEE Transactions on Industrial Electronics* (2019) 1–10.
- [15] W. L. Silva, A. M. N. Lima, A. Oliveira, Speed estimation of an induction motor operating in the nonstationary mode by using rotor slot harmonics, *IEEE Transactions on Instrumentation and Measurement* 64 (4) (2015) 984–994.
- [16] H. S. Zhao, Y. L. Wang, Y. Zhan, G. R. Xu, X. S. Cui, J. Wang, Practical model for energy consumption analysis of beam pumping motor systems and its energy-saving applications, *IEEE Transactions on Industry Applications* 54 (2) (2018) 1006–1016.
- [17] B. Y. Guo, X. H. Liu, X. H. Tan, Petroleum production engineering, a computer-assisted approach(Second Edition), Elsevier, 2017, 515-548.
- [18] M. B. Payán, J. M. R. Fernandez, J. M. M. Ortega, J. M. R. Santos, Techno-economic optimal power rating of induction motors, *Applied Energy* 240 (2019) 1031–1048.
- [19] Y. H. Li, M. S. Liu, J. Lau, B. Zhang, A novel method to determine the motor efficiency under variable speed operations and partial load conditions, *Applied energy* 144 (2015) 234–240.
- [20] Y. L. Luo, X. S. Cui, H. S. Zhao, D. Q. Zhang, Y. Luo, Y. L. Wang, A multifunction energy-saving device with a novel power-off control strategy for beam pumping motors, *IEEE Transactions on Industry Applications* 47 (4) (2011) 1605–1611.
- [21] A. B. Neely, K. E. Opal, H. A. Tripp, Power savings and load reductions on sucker rod pumping wells, in: SPE Annual Technical Conference and Exhibition, Society of Petroleum Engineers, 1989.

- [22] Z. M. Feng, J. J. Tan, Q. Li, X. Fang, A review of beam pumping energy-saving technologies, *Journal of Petroleum Exploration and Production Technology* 8 (1) (2018) 299–311.
- [23] X. M. Zhang, X. Yang, Z. Guo, Kinematics and dynamics analysis of drive mechanism of parallel four-bar energy-saving pumping unit, *Wuhan University journal of natural sciences* 17 (1) (2012) 73–78.
- [24] X. P. Li, K. Tian, C. H. Li, Y. Zhou, L. Y. Li, J. J. Hong, Liner electromagnetic oil pumping unit based on the principle of coil gun, *IEEE Transactions on Magnetics* 45 (1) (2009) 951–961.
- [25] S. G. Gibbs, Computing gearbox torque and motor loading for beam pumping units with consideration of inertia effects, *Journal of Petroleum Technology* 27 (9) (1975) 1153–1159.
- [26] W. M. Rossini, B. Alvarenga, I. E. Chabu, J. J. da Cruz, J. R. Cardoso, R. M. Sales, New concept for lifting in onshore oil wells, *IEEE Transactions on Industry Applications* 44 (4) (2008) 951–961.
- [27] G. Q. Han, H. Zhang, K. G. Ling, The optimization approach of casing gas assisted rod pumping system, *Journal of Natural Gas Science and Engineering* 32 (2016) 205–210.
- [28] W. C. Li, S. M. Dong, X. R. Sun, An improved sucker rod pumping system model and swabbing parameters optimized design, *Mathematical Problems in Engineering* 2018 (2018) 1–15.
- [29] S. Miska, A. Sharaki, J. M. Rajtar, A simple model for computer-aided optimization and design of sucker-rod pumping systems, *Journal of Petroleum Science and Engineering* 17 (3-4) (1997) 303–312.
- [30] X. F. Liu, Y. G. Qi, A modern approach to the selection of sucker rod pumping systems in cbm wells, *Journal of Petroleum Science and Engineering* 76 (3-4) (2011) 100–108.
- [31] L. Firu, T. Chelu, C. Militaru-Petre, A modern approach to the optimum design of sucker-rod pumping system, in: *SPE Annual Technical Conference and Exhibition*, Society of Petroleum Engineers, 2003, pp. SPE-84139-MS.
- [32] J. M. Lu, J. P. He, C. X. Mao, W. W. Wu, D. Wang, W. J. Lee, Design and implementation of a dual pwm frequency converter used in beam pumping unit for energy saving, *IEEE Transactions on Industry Applications* 50 (5) (2014) 2948–2956.
- [33] H. Wei, W. Wang, Intelligent balanced device and its sensing system for beam pumping units, *Sensors & Transducers* 182 (11) (2014) 62.



- [34] H. Zhao, Y. Wang, G. Chen, Y. Zhan, G. Xu, Precise determination of power-off time of intermittent supply technology based on fuzzy control for energy saving of beam pumping motor systems, *Electric Power Components and Systems* 46 (2) (2018) 197–207.
- [35] J. P. He, C. X. Mao, J. M. Lu, J. W. Yang, Design and implementation of an energy feedback digital device used in elevator, *IEEE Transactions on Industrial Electronics* 58 (10) (2011) 4636–4642.
- [36] L. H. Torres, L. Schntman, Sucker-rod pumping system of oil wells: modelling, identification and process control, *IFAC Proceedings Volumes* 46 (24) (2013) 260–265.
- [37] O. Bello, E. P. Dolberg, C. Teodoriu, K. H. D. D, Transformation of academic teaching and research: Development of a highly automated experimental sucker rod pumping unit, *Journal of Petroleum Science and Engineering* 190 (2020) 107087.
- [38] K. Palka, J. Czyz, Optimizing downhole fluid production of sucker-rod pumps with variable motor speed, *SPE Production & Operations* 24 (2) (2009) 346–352.
- [39] S. Al-Rbeawi, Integrated analysis of pressure response using pressure-rate convolution and deconvolution techniques for varied flow rate production in fractured formations, *Journal of Natural Gas Science and Engineering* 51 (2018) 195 – 209.
- [40] T. Gabor, Sucker-rod pumping handbook: production engineering fundamentals and long-stroke rod pumping, Gulf Professional Publishing, 2015, 57-246.
- [41] G. C. Shi, Z. M. Feng, D. S. Zhang, M. Z. Jiang, Influence of inertial load to dynamic characteristic of beam pumping units, *Oil Field Equipment* 44 (3) (2015) 34–37.
- [42] M. Z. Jiang, H. Wang, Y. Gao, Y. X. Dai, Study on changes of operating parameters of variable-speed driven pumping wells, *Oil Field Equipment* 39 (10) (2010) 4–7.
- [43] S. M. Dong, W. C. Li, X. F. Zhao, R. Zhao, Frequency conversion beam pumping system dynamic simulation and real time frequency optimization, *China Mechanical Engineering* 27 (12) (2016) 1585–1590.
- [44] W. C. Li, V. Vaziri, S. S. Aphale, S. M. Dong, M. Wiercigroch, Dynamics and frequency and voltage control of downhole oil pumping system, *Mechanical Systems and Signal Processing* 139 (2020) 106562.

- [45] B. Hansen, B. Tolbert, C. Vernon, J. D. Hedengren, Model predictive automatic control of sucker rod pump system with simulation case study, *Computers & Chemical Engineering* 121 (2019) 265 – 284.
- [46] S. M. Dong, *Computer Simulation Dynamic Parameters of Rod-Pumping System and System Optimization*, Beijing, China: Petroleum Industry Press, 2003.
- [47] P. C. Krause, O. Wasynczuk, S. D. Sudhoff, S. Pekarek, *Analysis of electric machinery and drive systems*, Vol. 2, Wiley Online Library, 2002.
- [48] B. S. Chen, *Electric Drive Automatic Control System*, Beijing, China: Machine Industry Press, 2003.
- [49] S. G. Gibbs, Predicting the behavior of sucker-rod pumping systems, *Journal of Petroleum Technology* 15 (7) (1963) 769–778.
- [50] Z. S. Chen, L. W. White, H. M. Zhang, Predicting sucker-rod pumping systems with fourier series, *SPE Production & Operations* 33 (4) (2018) 928–940.
- [51] M. M. Xing, Response analysis of longitudinal vibration of sucker rod string considering rod buckling, *Advances in Engineering Software* 99 (2016) 49–58.
- [52] B. Y. Zheng, X. W. Gao, X. Y. Li, Diagnosis of sucker rod pump based on generating dynamometer cards, *Journal of Process Control* 77 (2019) 76–88.
- [53] P. Xu, S. J. Xu, H. W. Yin, Application of self-organizing competitive neural network in fault diagnosis of suck rod pumping system, *Journal of Petroleum Science and Engineering* 58 (1-2) (2007) 43–48.
- [54] S. G. Gibbs, Design and diagnosis of deviated rod-pumped wells, *Journal of Petroleum Technology* 44 (7) (1992) 774–781.
- [55] B. Ordonez, A. Cudas, U. F. Moreno, A. Teixeira, Sucker-rod pumping system: simulator and dynamic level control using bottom hole pressure, in: *IEEE International Conference on Emerging Technologies and Factory Automation*, IEEE, Hamburg, Germany, 2008, pp. 282–289.